30th International Conference on General Relativity and Gravitation (GR30) / Amaldi 16 • Plenary Poster Presentation

Topological Microstates and Horizon Response of Rotating Black Holes in Scalar-Tensor Gravity

Xiatong Li and Jingxu Wu (wuxj@my.msu.ru) • *Faculty of Physics, Lomonosov Moscow State University, Moscow 119991, Russia*

1. Motivation & The Parity-Violating Switch

▸ Early-Universe PBHs & Topological Defects

Primordial black holes (PBHs) formed during radiation domination ($t_f \sim 2GH_f^{-1}$) coexist with cosmic strings, closed loops, and domain walls generated during early-universe symmetry-breaking phase transitions [1–7]. Modern PBH studies emphasize that black-hole mass M, dimensionless spin $\chi = a/M$, and local defect environments are coupled, model-dependent observables [8–17]. Rather than claiming an unconstrained ultraviolet quantum-gravity microstate count, we formulate a conditional effective-field-theory (EFT) problem:

If a rotating black hole is governed by a parity-violating scalar-tensor effective theory, can captured topological defects be organized into a computable horizon-sector response?

▸ Parity Selection Rule in dCS Gravity

In **dynamical Chern-Simons (dCS) gravity** [18–25], the scalar-Pontryagin coupling $\xi(\phi)\,{}^*RR$ obeys a strict geometric parity selection rule:

- **Static Spherically Symmetric Dormancy:** In terms of gravitoelectric ($E_{\mu\nu} = C_{\mu\alpha\nu\beta}u^\alpha u^\beta$) and gravitomagnetic ($B_{\mu\nu} = {}^*C_{\mu\alpha\nu\beta}u^\alpha u^\beta$) Weyl tensors, the Pontryagin density is ${}^*RR = -16E_{\mu\nu}B^{\mu\nu}$. For an exact Schwarzschild geometry:

$$ds^2 = -f(r)dt^2 + f(r)^{-1}dr^2 + r^2 d\Omega^2, \quad f(r) = 1 - \frac{2M}{r} \tag{1}$$

  the magnetic Weyl curvature vanishes identically ($B_{\mu\nu} = 0 \implies {}^*RR_{\rm Schw} = 0$). A non-rotating black hole does not source the scalar-Pontryagin sector at the classical background level.
- **Kerr Rotation as the Physical Switch:** Frame dragging on a rotating Kerr background activates $B_{\mu\nu} \neq 0$, turning on ${}^*RR \neq 0$ at $\mathcal{O}(\chi)$. Spin is therefore not a cosmetic detail—it is the physical switch that activates the scalar dipole, metric frame-dragging correction, Wald normal-bundle curvature charge, and compact boundary Chern-Simons sector.

▸ Perturbative Hierarchy & Architecture

Expanding around a constant background $\phi = \phi_0 + \varphi$ with $F_0 \equiv F(\phi_0)$ and $\xi_1 \equiv \xi_{,\phi}(\phi_0)$ in the controlled regime $\chi \ll 1$ and $\zeta_{\rm CS} \ll 1$:

$${}^*RR_{\rm Kerr} = \mathcal{O}(a) \;\Rightarrow\; \varphi = \mathcal{O}(a\lambda_{\rm CS}\xi_1) \;\Rightarrow\; \delta g^{\rm CS}_{t\varphi} = \mathcal{O}(a\lambda^2_{\rm CS}\xi_1^2) \tag{2}$$

Sector Stage	Physical Mechanism & Mathematical Output
1. Bulk Dipole	${}^*RR^{(1)} \propto a/r^7 \Rightarrow \Phi_{\rm phys}(r) \propto r^{-2}$, $\omega_{\rm CS} \propto r^{-6}$
2. Wald Charge	Normal curvature $F_N = 2\,\mathrm{Im}\,\Psi_2$ & flux $\dot{S}^{(2)}_{\rm topo}$
3. Boundary CS	Projection $\mathcal{P}_{\mathcal{H}} \to SU(2)_k$, projector $\Gamma^{\rm phys}_K \leq 1$
4. Observables	Capture prior $\mu_{\rm cap}$, $T_{\rm env}$ shift & EMRI $\Delta\Psi_{R/L}$

Key Structural Theorem: Spin-Switched Parity Violation
Static black holes are completely blind to the Pontryagin sector (${}^*RR_{\rm Schw} = 0$). Angular momentum $J = Ma$ acts as the universal switch that activates the dipolar scalar cloud $\Phi_{\rm phys}(r) \propto a\lambda_{\rm CS}\xi_1$ and seeds all horizon responses at $\mathcal{O}(\chi\zeta_{\rm CS})$.

2. Covariant Action & Modified Field Equations

▸ Unique Planck-Normalized Action & Dimensional Analysis

We maintain one Planck-normalized convention throughout all bulk and boundary derivations ($c = \hbar = 1$):

$$S = \int \frac{d^4x\sqrt{-g}}{16\pi G}\left[F(\phi)R - \frac{1}{2}\nabla_\mu\phi\nabla^\mu\phi - V(\phi) + \frac{\lambda_{\rm CS}}{4}\xi(\phi)\,{}^*RR\right] \tag{3}$$

where $\alpha_{\rm dCS} \equiv \lambda_{\rm CS}$. Because the scalar kinetic term is inside the same overall $(16\pi G)^{-1}$ factor as the Einstein term, the exact dimensions are:

$$\dim G = \dim \alpha_{\rm dCS} = L^2, \quad \dim V = L^{-2}, \quad \dim\phi = \dim F = \dim\xi = 1 \tag{4}$$

The parity-odd Pontryagin curvature density in abstract-index notation and the right-handed Levi-Civita orientation are fixed by:

$${}^*RR = \frac{1}{2}\epsilon^{abcd}R_{cdpq}R_{abef}g^{ep}g^{fq}, \quad \epsilon^{tr\theta\varphi} = (-g)^{-1/2} \tag{5}$$

▸ Coupled Metric & Scalar Field Equations

Variation of S with respect to $g^{\mu\nu}$ and ϕ yields the exact covariant system:

$$F(\phi)G_{\mu\nu} - \nabla_\mu\nabla_\nu F(\phi) + g_{\mu\nu}\Box F(\phi) + \lambda_{\rm CS}C_{\mu\nu} = \frac{1}{2}T^{(\phi)}_{\mu\nu} \tag{6}$$

$$\Box\phi - V_{,\phi} + F_{,\phi}R + \frac{\lambda_{\rm CS}}{4}\xi_{,\phi}\,{}^*RR = 0 \tag{7}$$

where the conventional scalar stress-energy tensor $T^{(\phi)}_{\mu\nu} \equiv -\frac{2}{\sqrt{-g}}\frac{\delta(\sqrt{-g}\mathcal{L}_\phi)}{\delta g^{\mu\nu}}$ and the 4D trace-free Cotton tensor $C_{\mu\nu}$ are:

$$T^{(\phi)}_{\mu\nu} = \nabla_\mu\phi\nabla_\nu\phi - \frac{1}{2}g_{\mu\nu}\nabla_\rho\phi\nabla^\rho\phi - g_{\mu\nu}V(\phi) \tag{8}$$

$$C^{\mu\nu} = (\nabla_\rho\xi)\epsilon^{\rho\sigma\alpha(\mu}\nabla_\alpha R^{\nu)}{}_\sigma + (\nabla_\rho\nabla_\sigma\xi)\,{}^*R^{\rho(\mu\nu)\sigma} \tag{9}$$

▸ Ricci-Flat Perturbative Reduction (Appendix A)

Expanding $\phi = \phi_0 + \varphi$ around a Ricci-flat Schwarzschild background ($R_{\mu\nu} = 0$, $R = 0$), the Ricci-derivative piece $(\nabla_\rho\xi)\epsilon^{\rho\sigma\alpha(\mu}\nabla_\alpha R^{\nu)}{}_\sigma$ vanishes identically at leading order, reducing the metric Cotton source in the $t\varphi$ sector to:

$$C^{\mu\nu} \simeq \xi_1(\nabla_\rho\nabla_\sigma\varphi)\,{}^*R^{\rho(\mu\nu)\sigma}, \quad \xi_1 \equiv \left.\frac{d\xi}{d\phi}\right|_{\phi_0} \tag{10}$$

Orientation & Parity Invariance Check
A simultaneous reversal of the Levi-Civita convention ($\epsilon^{tr\theta\varphi} \to -\epsilon^{tr\theta\varphi}$) and the Cotton tensor definition reverses the sign of $\delta g^{\rm CS}_{t\varphi}$ while leaving $|\zeta_{\rm CS}|$ and the perturbative consistency of the field equations invariant.

3. Slow-Rotation Dipolar Scalar Solution

▸ Linear Spin Expansion & Dipolar Source

We write the slowly rotating stationary metric to first order in the spin book-keeping parameter ϵ (set to $\epsilon = 1$ after linear reduction):

$$ds^2 = -f(r)dt^2 + f(r)^{-1}dr^2 + r^2d\Omega^2 - 2\epsilon r^2\sin^2\theta\,\omega(r)\,dt\,d\varphi \tag{11}$$

At zeroth order in $\lambda_{\rm CS}$, the $t\varphi$ Einstein tensor vanishes for the Kerr dragging profile:

$$G^{(1)}_{t\varphi} = \frac{r-2M}{2}\left[r\omega'' + 4\omega'\right]\sin^2\theta = 0 \implies \omega_{\rm Kerr}(r) = \frac{2Ma}{r^3} \tag{12}$$

Evaluating the Pontryagin density on this linear Kerr background yields an exact dipolar ($l = 1$) source:

$${}^*RR^{(1)}_{\rm Kerr} = \frac{288M^2a\cos\theta}{r^7} \tag{13}$$

Separating variables as $\varphi(r,\theta) = \Phi(r)\cos\theta$ reduces the scalar wave equation to:

$$f(r)\Phi'' + \frac{2(r-M)}{r^2}\Phi' - \left(\frac{2}{r^2} + m^2_\phi\right)\Phi + \frac{72M^2a\lambda_{\rm CS}\xi_1}{r^7} = 0 \tag{14}$$

For a massless scalar ($m_\phi = 0$), horizon regularity at $r_+ = 2M$ and decay at infinity uniquely fix:

$$\Phi_{\rm phys}(r) = \frac{5a\lambda_{\rm CS}\xi_1}{8Mr^2}\left(1 + \frac{2M}{r} + \frac{18M^2}{5r^2}\right) = \frac{A_2}{r^2} + \frac{A_3}{r^3} + \frac{A_4}{r^4} \tag{15}$$

with $A_2 = \frac{5a\lambda_{\rm CS}\xi_1}{8M}$, $A_3 = \frac{5a\lambda_{\rm CS}\xi_1}{4}$, and $A_4 = \frac{9Ma\lambda_{\rm CS}\xi_1}{4}$. At the horizon $r_+ = 2M$, $\Phi_{\rm phys}(2M) = \frac{73}{64}\frac{a\lambda_{\rm CS}\xi_1}{M^3}$, whereas the homogeneous solution $Q_1(r/M-1) \sim \ln(1-2M/r)$ diverges and is excluded by horizon regularity.

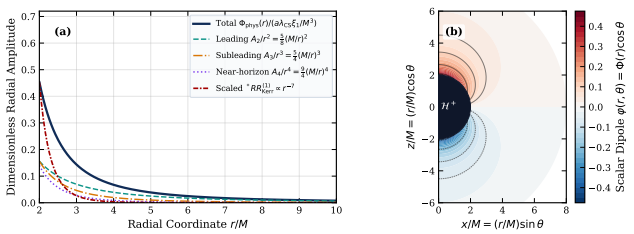


Figure 1: (a) Radial decay of $\Phi_{\rm phys}(r)$, multipole pieces A_n/r^n, and scaled ${}^*RR^{(1)}_{\rm Kerr} \propto r^{-7}$. (b) Poloidal cross-section $(x/M, z/M)$ of the scalar dipole cloud $\varphi(r,\theta)$ around $\mathcal{H}^+$.

4. Cotton Tensor Backreaction & Frame Dragging

▸ Explicit Cotton Tensor Metric Source

Before substituting the explicit radial profile $\Phi_{\rm phys}(r)$, the off-diagonal $t\varphi$ component of the Cotton tensor for any axisymmetric dipolar scalar $\varphi = \Phi(r)\cos\theta$ on the slowly rotating background takes the exact differential form (Appendix B):

$$C_{t\varphi} = \frac{3M\xi_1(r-2M)}{r^5}\left[r\Phi'(r) - \Phi(r)\right]\sin^2\theta \tag{16}$$

Substituting $\Phi_{\rm phys}(r)$ and its radial derivative $\Phi'_{\rm phys}(r) = -\frac{5a\lambda_{\rm CS}\xi_1}{4Mr^3}\left(1+\frac{3M}{r}+\frac{36M^2}{5r^2}\right)$ yields the physical parity-violating metric source:

$$C^{\rm phys}_{t\varphi} = -\frac{15a\lambda_{\rm CS}\xi_1^2}{8r^9}(r-2M)\left(18M^2+8Mr+3r^2\right)\sin^2\theta \tag{17}$$

▸ Radial ODE & Polynomial Frame-Dragging Solution

Inserting $C^{\rm phys}_{t\varphi}$ into the $t\varphi$ component of the modified Einstein equation yields $(r-2M)\mathcal{E}_{t\varphi}[\omega_{\rm CS}] = 0$. Factoring out the common horizon zero $(r-2M)$ outside the horizon $(r > 2M)$ gives the reduced 2nd-order radial ODE:

$$\mathcal{E}_{t\varphi}[\omega] \equiv \frac{F_0}{2}\left(r\omega'' + 4\omega'\right) - \frac{15a\lambda_{\rm CS}^2\xi_1^2\left(18M^2+8Mr+3r^2\right)}{8r^9} = 0 \tag{18}$$

Solving with the asymptotically decaying polynomial ansatz $\omega_{\rm CS}(r) = B_6 r^{-6} + B_7 r^{-7} + B_8 r^{-8}$ fixes the exact algebraic coefficients:

$$B_6 = \frac{5a\lambda_{\rm CS}^2\xi_1^2}{8F_0}, \quad B_7 = \frac{15Ma\lambda_{\rm CS}^2\xi_1^2}{14F_0}, \quad B_8 = \frac{27M^2a\lambda_{\rm CS}^2\xi_1^2}{16F_0} \tag{19}$$

Equivalently, in common-denominator form:

$$\omega_{\rm CS}(r) = \frac{a\lambda_{\rm CS}^2\xi_1^2}{112F_0r^8}\left(70r^2+120Mr+189M^2\right) \tag{20}$$

Thus the full frame-dragging angular velocity and $g_{t\varphi}$ metric component are:

$$\omega(r) = \frac{2Ma}{r^3} + \frac{5a\lambda_{\rm CS}^2\xi_1^2}{8F_0r^6}\left(1+\frac{12M}{7r}+\frac{27M^2}{10r^2}\right) \tag{21}$$

$$g_{t\varphi} = -\frac{2Ma}{r}\sin^2\theta - \frac{5a\lambda_{\rm CS}^2\xi_1^2}{8F_0r^4}\left(1+\frac{12M}{7r}+\frac{27M^2}{10r^2}\right)\sin^2\theta \tag{22}$$

Symbolic Verification via Mathematica + xAct/xPert

All three exact operator identities $G^{(1)}_{t\varphi}[\omega_{\rm Kerr}] = 0$, $\mathcal{E}_\phi[\Phi_{\rm phys}] = 0$, and $\mathcal{E}_{t\varphi}[\omega_{\rm CS}] = 0$ were verified symbolically by direct tensor reduction in `xAct/xPert` (Appendix C).

5. Horizon Angular Velocity Shift & EFT Domain

▸ Universal Dimensionless Scaling

Introducing the dimensionless spin $\chi \equiv a/M \ll 1$ and the standard small-coupling parameter $\zeta_{\rm CS}$, the relative metric correction and horizon angular velocity shift ($\Omega_H^{\rm GR} \simeq a/(4M^2)$ at $r_H \simeq 2M$) take the universal form:

$$\frac{\delta g^{\rm CS}_{t\varphi}}{g^{\rm Kerr}_{t\varphi}} = \frac{5}{16}\zeta_{\rm CS}\left(\frac{M}{r}\right)^3\left(1+\frac{12M}{7r}+\frac{27M^2}{10r^2}\right) \tag{23}$$

$$\delta\Omega_H = \frac{709}{28672}\frac{a\alpha^2_{\rm dCS}\xi_1^2}{F_0M^6} \implies \frac{\delta\Omega_H}{\Omega_H^{\rm GR}} = \frac{709}{7168}\frac{\alpha^2_{\rm dCS}\xi_1^2}{F_0M^4} = \frac{709}{7168}\zeta_{\rm CS} \tag{24}$$

▸ EFT Breakdown Scale & Cutoff Physics

- **Characteristic EFT Mass Scale:** We define the dCS threshold mass and normalized mass ratio:

$$M_{\rm dCS} \equiv \left(\frac{\alpha^2_{\rm dCS}\xi_1^2}{F_0}\right)^{1/4}, \quad x_M \equiv \frac{M}{M_{\rm dCS}} \implies \zeta_{\rm CS} = x_M^{-4} \tag{25}$$

- **Strict EFT Cutoff ($x_M \geq 3$):** Perturbative control requires $\zeta_{\rm CS} \ll 1$. At $x_M = 3$, $\zeta_{\rm CS} = 3^{-4} \approx 0.0123$, whereas for $x_M < 3$ the steep x_M^{-4} growth drives higher-derivative operators out of control.
- **Exclusion of Uncontrolled Endpoints:** Claims of Planckian remnants at $M \sim M_{\rm dCS}$ lie inside the uncontrolled region $x_M < 3$ and cannot be inferred from the leading EFT alone.

▸ Quantitative EFT Benchmark Regimes

Mass Ratio x_M	$\zeta_{\rm CS} = x_M^{-4}$	$\delta\Omega_H/\Omega_H^{\rm GR}$	Perturbative Status
$x_M = 10.0$	1.00×10^{-4}	9.89×10^{-6}	Deep EFT Control
$x_M = 5.0$	1.60×10^{-3}	1.58×10^{-4}	Controlled Inspiral
$x_M = 3.0$ (Cutoff)	1.23×10^{-2}	1.22×10^{-3}	EFT Validity Boundary
$x_M < 1.78$	> 0.10	$> 9.89\times10^{-3}$	Derivative Breakdown

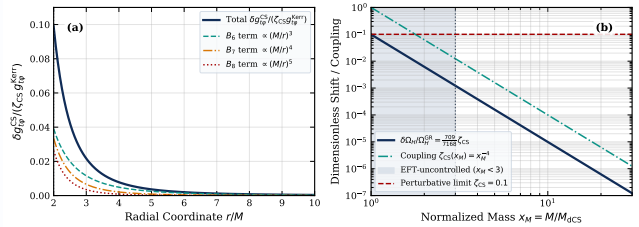


Figure 2: (a) Radial profile of $\delta g^{\rm CS}_{t\varphi}/(\zeta_{\rm CS} g^{\rm Kerr}_{t\varphi})$ decomposed into B_6, B_7, B_8 multipole terms outside $r_+ \simeq 2M$. (b) Log-log scaling of $\delta\Omega_H/\Omega_H^{\rm GR} \propto x_M^{-4}$ and $\zeta_{\rm CS}(x_M)$, showing the controlled EFT domain ($x_M \geq 3$) vs. shaded uncontrolled band ($x_M < 3$).

6. Exact Normalization & Literature Dictionary

▸ Comparison with Standard Slow-Rotation Literature

In Refs. [20–24] (Yunes-Pretorius, Sopuerta-Yunes, Yagi-Yunes-Tanaka, Stein), the dCS action is written with separate pre-factors $\kappa = (16\pi G)^{-1}$ and β:

$$S_{\rm std} = \int d^4x\sqrt{-g}\left[\kappa F_0 R - \frac{\beta}{2}\nabla_\mu\vartheta\nabla^\mu\vartheta + \frac{\alpha_{\rm std}}{4}\vartheta\, {}^*RR\right] \tag{26}$$

Setting $\vartheta = \phi$, $\beta = \kappa$, $\kappa_E = \kappa F_0$, and $\alpha_{\rm std} = \kappa\alpha_{\rm dCS}\xi_1$ yields exact term-by-term equivalence between our expressions and the Yunes-Pretorius-Stein slow-rotation profile.

Table 1: Exact convention dictionary between our Planck-normalized action and standard slow-rotation dCS literature.

This Work (Planck Normalized)	Standard dCS Literature
Pre-factor: $(16\pi G)^{-1}$ on all terms	$\kappa_E = \kappa F_0$; $\beta = \kappa$ outside
Linearized Coupling: $\alpha_{\rm dCS}\xi_1 = \lambda_{\rm CS}\xi_1$	$\alpha_{\rm std}/\kappa$ for canonical $\vartheta = \phi$
Einstein Equation RHS: $\frac{1}{2}T^{(\phi)}_{\mu\nu}$	$8\pi G T^{(\vartheta)}_{\mu\nu}$, full $F,_\phi R$ source
Wald Area Term: $S_F = (4G)^{-1}\oint\sqrt{q}F(\phi)$	Directly normalized by F_0
Small Coupling: $\zeta_{\rm CS} = \frac{\alpha^2_{\rm dCS}\xi_1^2}{F_0M^4}$	$\zeta_{\rm std} = \frac{\alpha^2_{\rm std}}{\kappa_E\beta M^4}$
Radial Shift: Eq. (22) for $\delta g^{\rm CS}_{t\varphi}/g^{\rm Kerr}_{t\varphi}$	Matches Yunes-Stein polynomial

▸ Radial & Angular Structure of the Cotton Source

The physical Cotton source $C^{\rm phys}_{t\varphi}$ carries an explicit factor $(r-2M)$, vanishing on the background horizon $r_+ = 2M$ and peaking at $r \approx 2.38M$ before decaying as r^{-6} at spatial infinity:

Field	Leading	Horizon $r_+ = 2M$	Parity / Spin
${}^*RR^{(1)}_{\rm Kerr}$	$288M^2a\cos\theta/r^7$	$\frac{9}{4}(a/M^5)\cos\theta$	Odd / $\mathcal{O}(\chi)$
$\Phi_{\rm phys}(r)$	$\frac{5}{8}a\lambda_{\rm CS}\xi_1/(Mr^2)$	$\frac{73}{64}a\lambda_{\rm CS}\xi_1/M^3$	Odd / $\mathcal{O}(\chi\zeta_{\rm CS}^{1/2})$
$\omega_{\rm CS}(r)$	$\frac{5}{8}a\lambda^2_{\rm CS}\xi_1^2/(F_0r^6)$	$\frac{709}{28672}(a/M^2)\zeta_{\rm CS}$	Even / $\mathcal{O}(\chi\zeta_{\rm CS})$

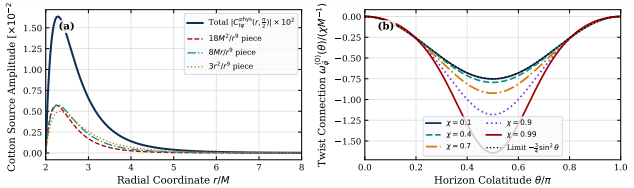


Figure 3: (a) Equatorial radial profile of the Cotton tensor $|C^{\rm phys}_{t\varphi}(r,\pi/2)|$ decomposed into $18M^2/r^9$, $8Mr/r^9$, and $3r^2/r^9$ pieces. (b) Horizon twist connection $\omega^{(0)}_{\tilde\varphi}(\theta)/(\chi M^{-1})$ across colatitude θ/π for spins $\chi \in [0.1, 0.99]$ vs. slow-rotation limit $-\frac{3}{4}\sin^2\theta$.

7. Covariant Phase Space & Normal-Bundle Charge

▸ Iyer-Wald Horizon Noether Charge

On a spacelike cross-section B_v of the future event horizon $\mathcal{H}^+$, we introduce future-directed null normals ℓ^a and n^a satisfying $\ell^a n_a = -1$ and $\ell^a \ell_a = n^a n_a = 0$, inducing the 2-metric $q_{ab} = g_{ab} + \ell_a n_b + n_a \ell_b$ and binormal $\epsilon_{ab} = 2\ell_{[a} n_{b]}$. In the Iyer-Wald formalism [35–39], the horizon entropy functional is:

$$S_{\rm Wald} = -2\pi \oint_{B_v} d^2x \sqrt{q}\, E_R^{abcd} \epsilon_{ab} \epsilon_{cd}, \quad E_R^{abcd} \equiv \frac{\partial \mathcal{L}}{\partial R_{abcd}} \tag{27}$$

▸ Normal-Bundle Connection & Boost Invariance

Define the intrinsic normal-bundle connection (twist 1-form) on B_v:

$$\omega_A = -n_a q_A{}^b \nabla_b \ell^a, \quad A, B \in \{\theta, \tilde{\varphi}\} \tag{28}$$

Under a local boost of the null frame ($\ell^a \to e^{\chi} \ell^a$, $n^a \to e^{-\chi} n^a$), ω_A transforms as an abelian gauge connection $\omega_A \to \omega_A + D_A \chi$. Consequently, its exterior curvature 2-form $\mathcal{F}_{AB} = 2D_{[A}\omega_{B]}$ and scalar dual:

$$F_N \equiv \frac{1}{2} \tilde{\epsilon}^{AB} \mathcal{F}_{AB} = \tilde{\epsilon}^{AB} D_A \omega_B \tag{29}$$

are **strictly boost-invariant**. By the codimension-two Ricci equation, contracting the Riemann derivative of $\frac{\alpha}{64\pi G} \xi(\phi)\, {}^*RR$ with $\epsilon_{ab}\epsilon_{cd}$ projects the spacetime curvature onto the normal bundle, yielding the total Wald entropy:

$$S_{\rm Wald} = S_F + S_{\rm topo} = \frac{1}{4G} \oint_{B_v} d^2x \sqrt{q}\, [F(\phi) + \alpha\, \xi(\phi) F_N] \tag{30}$$

▸ Area Dissipation vs. Topological Angular Transport

Property	Einstein Area S_F vs. Normal-Bundle $S_{\rm topo}$
Parity Transformation	S_F: Parity-even $(+1)$; $S_{\rm topo}$: Parity-odd (-1)
Geometric Origin	S_F: Intrinsic area $\sqrt{q}$; $S_{\rm topo}$: Normal curvature F_N
Stationary Smooth Kerr	$S_F = \frac{A_H}{4G} F_0 > 0$; $S^{(0)}_{\rm topo} = 0$ (by Stokes' theorem)
Nonzero Stationary Cond.	Requires punctures, framing, or non-trivial patching
Dynamical Evolution	$\dot{S}_A \propto \sigma_{AB}\sigma^{AB} \geq 0$; $\dot{S}^{(2)}_{\rm topo}$ changes sign at $\omega = m\Omega_H$

Geometric vs. Area Entropy
Unlike the Bekenstein-Hawking area term S_F, $S_{\rm topo}$ is an orientation-sensitive Wald-Noether charge measuring the scalar-weighted curvature of the horizon normal bundle.

8. Explicit Evaluation on the Kerr Horizon

▸ Kerr Horizon Geometry & Twist Connection

For a stationary Kerr horizon with generator $\ell^a \partial_a = \partial_v + \Omega_H \partial_{\tilde{\varphi}}$, horizon radius $r_\pm = M \pm \sqrt{M^2 - a^2}$, angular velocity $\Omega_H = \frac{a}{r_+^2 + a^2}$, and surface gravity $\kappa = \frac{r_+ - r_-}{2(r_+^2 + a^2)}$, the intrinsic cross-section metric is:

$$q^{(0)}_{AB} dx^A dx^B = \Sigma_+ d\theta^2 + \Sigma_+^{-1} (r_+^2 + a^2)^2 \sin^2\theta d\tilde{\varphi}^2 \tag{31}$$

where $\Sigma_+ = r_+^2 + a^2 \cos^2\theta$ and $\sqrt{q_0} = (r_+^2 + a^2)\sin\theta$. In a regular northern gauge patch ($\omega^{(0)}_\theta = 0$), the rotation 1-form is:

$$\omega^{(0)}_{\tilde{\varphi}}(\theta) = \frac{M(r_+^2 + a^2)}{a} \left[\frac{a^2 \cos^2\theta - r_+^2}{(r_+^2 + a^2\cos^2\theta)^2} - \frac{a^2 - r_+^2}{(r_+^2 + a^2)^2} \right]$$
$$= -\frac{3a}{4M} \sin^2\theta + \mathcal{O}(a^3/M^3) \quad \text{(regular as } a \to 0) \tag{32}$$

▸ Exact Curvature Scalar & Vanishing Smooth Integral

Taking the 2D curl $F^{(0)}_N = \frac{1}{\sqrt{q_0}} \partial_\theta \omega^{(0)}_{\tilde{\varphi}}$ gives the exact Kerr normal-bundle curvature:

$$F^{(0)}_N(\theta) = 2\,\mathrm{Im}\, \Psi_2^{\rm Kerr}\big|_{r_+} = -\frac{2Ma\cos\theta(3r_+^2 - a^2\cos^2\theta)}{(r_+^2 + a^2\cos^2\theta)^3} \tag{33}$$

where $\Psi_2^{\rm Kerr} = -M(r - ia\cos\theta)^{-3}$ and $F^{(0)}_N \simeq -\frac{3a}{8M^3}\cos\theta$ at small spin. On an unpunctured horizon with constant ξ_H, Stokes' theorem gives $S^{(0)}_{\rm topo} = \frac{\alpha \xi_H}{4G} \oint \sqrt{q_0} F^{(0)}_N d^2x = 0$. Nonzero stationary charge requires **defect punctures or framing**!

▸ Southern Patch Gluing & Defect Punctures

On a smooth sphere S^2, northern ($\omega^N_{\tilde{\varphi}}$) and southern ($\omega^S_{\tilde{\varphi}}$) gauge patches glue via a regular $SO(1,1)$ boost on the equator. When cosmic strings puncture B_v at $\{\theta_p, \tilde{\varphi}_p\}$, Stokes' theorem acquires boundary holonomies around the punctures, rendering $S_{\rm topo} \neq 0$.

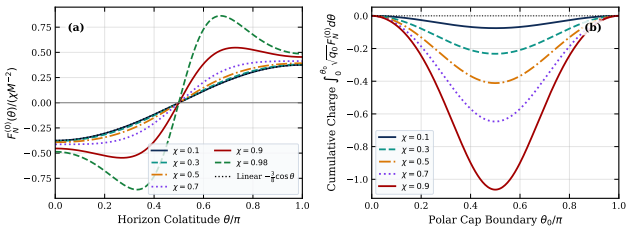


Figure 4: (a) Exact Kerr normal-bundle curvature profile $F^{(0)}_N(\theta)/(\chi M^{-2})$ across colatitude θ/π for spins $\chi \in [0.1, 0.98]$. (b) Cumulative polar-cap charge $\int_0^{\theta_0} \sqrt{q_0} F^{(0)}_N d\theta$, showing exact global cancellation at $\theta_0 = \pi$.

9. Teleological Raychaudhuri Flux & First Law

▸ Teleological Raychaudhuri Integration

Along the null generator ($\dot{X} \equiv \mathcal{L}_\ell X$), the expansion $\theta = q^{ab}\nabla_a \ell_b$ and shear σ_{AB} obey:

$$\dot{\theta} - \kappa\theta = -\frac{1}{2}\theta^2 - \sigma_{AB}\sigma^{AB} - 8\pi G T^{\rm eff}_{\ell\ell} \tag{34}$$

$$8\pi G T^{\rm eff}_{ab} = F^{-1} \left[\frac{1}{2} T^{(\phi)}_{ab} + \nabla_a \nabla_b F - g_{ab} \Box F - \alpha C_{ab} \right] \tag{35}$$

Imposing future regularity eliminates growing modes ($\theta^{(1)} = 0$) and gives:

$$\theta^{(2)}(v) = \int_v^\infty dv'\, e^{\kappa(v-v')} \left[\sigma^{(1)}_{AB} \sigma^{AB(1)} + 8\pi G T^{\rm eff(2)}_{\ell\ell} \right]_{v'} \tag{36}$$

▸ Second-Order Topological Flux & Deformed Boundary Condition

Integrating by parts on B_v gives $\dot{S}_{\rm topo} = \frac{\alpha}{4G} \oint d^2x \sqrt{q_0} [(\dot{\xi} + \xi\theta) F_N - \tilde{\epsilon}^{AB} (D_A \xi) \dot{\omega}_B]$. Expanding to 2nd order around Kerr yields:

$$\dot{S}^{(2)}_{\rm topo} = \frac{\alpha}{4G} \oint d^2x \sqrt{q_0} \Big[(\xi_0' \dot{\phi}^{(2)} + \xi_0 \theta^{(2)}) F^{(0)}_N + \frac{\xi_0''}{2} \partial_v (\phi^{(1)})^2 F^{(0)}_N$$
$$+ \xi_0 \dot{F}^{(2)}_N + \xi_0' (\dot{\phi}^{(1)} F^{(1)}_N + \phi^{(1)} \dot{F}^{(1)}_N - \tilde{\epsilon}^{AB} D_A \phi^{(1)} \dot{\omega}^{(1)}_B) \Big] \tag{37}$$

In the dynamical horizon first law $\frac{dM}{dv} = \frac{\kappa}{8\pi G}\frac{dA}{dv} + \Omega_H \frac{dJ}{dv} + \mathcal{F}_F + \mathcal{F}_{\rm topo} + \mathcal{P}_{\rm out}$, where $\mathcal{F}_F = T_H \left[\frac{1}{4G} \oint d^2x \sqrt{q} (F\theta + \dot{F}) - \frac{1}{4G}\frac{dA}{dv} \right]$ (vanishing for minimally coupled dCS $F = 1$), an EMRI mode $\phi^{(1)}_{\ell m\omega} \propto e^{-i(\omega - m\Omega_H)v + im\tilde{\varphi}}$ satisfies $\dot{\phi}^{(1)}_{\ell m\omega} = -ik_H \phi^{(1)}_{\ell m\omega}$ ($k_H \equiv \omega - m\Omega_H$). The secular 2nd-order radiative flux and deformed ingoing horizon condition are:

$$\langle \mathcal{F}^{(2)}_{\rm topo} \rangle = \frac{\kappa \alpha \xi_0'}{8\pi G} \oint \sqrt{q_0} [\langle \dot{\phi}^{(1)} F^{(1)}_N \rangle - \tilde{\epsilon}^{AB} \langle D_A \phi^{(1)} \dot{\omega}^{(1)}_B \rangle] \tag{38}$$

$$(\partial_{r_*} + ik_H) \Psi_{\ell m\omega}\big|_{r_+} = \alpha \xi_0' \mathcal{B}_{\ell m\omega} [\phi_{\ell m\omega}, h_{\ell m\omega}] \tag{39}$$

Thermodynamic Insight: Superradiant Sign Reversal
Unlike positive-definite shear dissipation $\sigma_{AB}\sigma^{AB} \geq 0$, the parity-odd flux $\langle \mathcal{F}^{(2)}_{\rm topo} \rangle \propto k_H$ reverses sign across the superradiant threshold $\omega = m\Omega_H$.

10. Pullback of the Lorentz Chern-Simons Current

▸ Bulk-to-Boundary Action Decomposition

Defining the 1st-order trace $\mathrm{Tr}(R \wedge R) \equiv \frac{1}{16\pi} {}^*RR\,\epsilon_4 = d\mathcal{Q}_3(\omega)$ with Lorentz connection ω^{IJ} and Chern-Simons 3-form $\mathcal{Q}_3(\omega) = \mathrm{Tr}\left(\omega \wedge d\omega + \frac{2}{3}\omega \wedge \omega \wedge \omega\right)$, integration by parts on a spacetime $\mathcal{M}$ with inner horizon boundary $\mathcal{H}$ decomposes the parity-odd action into:

$$I_P = \frac{\alpha}{4G}\int_{\partial\mathcal{M}} \xi\,\mathcal{Q}_3(\omega) - \frac{\alpha}{4G}\int_{\mathcal{M}} d\xi \wedge \mathcal{Q}_3(\omega) \tag{40}$$

In the adiabatic horizon regime ($D_A\xi_H = 0$, $\xi_H \equiv \xi(\phi_H) = \text{const}$ on B_v), the horizon boundary action is $I^{\mathrm{top}}_{\mathcal{H}} = \frac{\alpha\xi_H}{4G}\int_{\mathcal{H}} \mathcal{Q}_3(\omega)\big|_{\mathcal{H}}$.

▸ Compact Projection Prescription $\mathcal{P}_{\mathcal{H}}$

A compact $SU(2)_k$ boundary theory is defined as an effective boundary completion fixed by the prescription data [40–48]:

$$\mathcal{P}_{\mathcal{H}} = \left\{e|_{\mathcal{H}},\, \tau^I,\, P_{\mathrm{comp}},\, \mathrm{Tr},\, \ell_H\right\} \tag{41}$$

where $e|_{\mathcal{H}}$ is the horizon tetrad, τ^I fixes the internal time gauge, ℓ_H sets the connection scale, and P_{comp} projects the complex connection onto its real compact $SU(2)$ section:

$$A^{(C)}_i = \left(\omega_i{}^a + i\ell_H^{-1} e_i{}^a\right) T_a, \quad A^{(R)} = P_{\mathrm{comp}} A^{(C)} \tag{42}$$

with $\mathrm{Tr}(T_a T_b) = \frac{1}{2}\delta_{ab}$ and $\mathrm{CS}_3[A^{(R)}] = \mathrm{Tr}\big(A^{(R)} \wedge dA^{(R)} + \frac{2}{3}A^{(R)} \wedge A^{(R)} \wedge A^{(R)}\big)$. Pulling back $\mathcal{Q}_3(\omega)$ onto $\mathcal{H}$ gives $\mathcal{Q}_3(\omega)\big|_{\mathcal{H}} = \eta_H\,\mathrm{CS}_3[A^{(R)}] + d\mathcal{B}_{\mathcal{H}} + \mathcal{Q}_{\mathrm{noncompact}}$. By parity and vanishing at $J = 0$, the leading dimensionless projection factor is $\eta_H = 4\gamma_H \frac{J}{Mr_+} + \mathcal{O}(a^3/M^3)$, yielding the matched compact boundary action and classical effective level:

$$I^{\mathrm{top}}_{\mathcal{H}} = \frac{k^{\mathrm{cl}}_{\mathrm{eff}}}{4\pi}\int_{\mathcal{H}} \mathrm{CS}_3[A^{(R)}] + I_{\mathrm{noncompact}} + I_{\mathrm{exact}} \tag{43}$$

$$k^{\mathrm{cl}}_{\mathrm{eff}} = 4\pi\gamma_H \frac{\alpha}{G}\xi(\phi_H)\frac{J}{Mr_+} + \mathcal{O}\left(\frac{a^3}{M^3}\right) \tag{44}$$

▸ Lorentzian dCS vs. Compact $SU(2)_k$ Completion

Boundary Ingredient	Physical & Mathematical Role
4D dCS Action I_P	Supplies exact Lorentz CS current $\mathcal{Q}_3(\omega)$
Projector P_{comp}	Extracts compact $SU(2)$ connection $A^{(R)}$
Noncompact $\mathcal{Q}_{\mathrm{noncompact}}$	Governs dissipative Lorentzian shear/flux
Combined Scale Λ_H	$\Lambda_H \equiv \gamma_H\alpha\xi_H/G$ controls physical level $k^{\mathrm{cl}}_{\mathrm{eff}}$

Conditional Boundary Prescription
The integer $k \in \mathbb{Z}_{\geq 1}$ is not a quantization of the classical bulk coupling α_{dCS}; it labels admissible unitary $SU(2)_k$ boundary sectors after fixing $\mathcal{P}_{\mathcal{H}}$, parameterized by $\Lambda_H \equiv \gamma_H\alpha\xi_H/G$.

11. Presymplectic Matching & Knot Atlas

▸ Covariant Symplectic Matching

From $\delta\mathcal{Q}_3 = 2\mathrm{Tr}(\delta\omega\wedge R) + d\mathrm{Tr}(\omega\wedge\delta\omega)$, the horizon symplectic potential and antisymmetrized presymplectic form are:

$$\Theta^P_{\mathcal{H}}(\delta) = \frac{\alpha}{2G}\xi_H\,\mathrm{Tr}(\delta\omega \wedge R) + \frac{\alpha}{4G}d\left[\xi_H\,\mathrm{Tr}(\omega \wedge \delta\omega)\right] + \Theta_{\nabla\xi} \tag{45}$$

$$\Omega^P_{\mathcal{H}}(\delta_1,\delta_2) = \frac{\alpha}{2G}\xi_H\int_{B_v} \mathrm{Tr}\left(\delta_1\omega \wedge \delta_2\omega - \delta_2\omega \wedge \delta_1\omega\right) + \Omega_{\nabla\xi} \tag{46}$$

Under P_{comp}, $\Omega^P_{\mathcal{H}}$ matches the canonical $SU(2)$ Chern-Simons symplectic form:

$$\Omega^P_{\mathcal{H}}\big|_{\mathrm{compact}} = \frac{k^{\mathrm{cl}}_{\mathrm{eff}}}{4\pi}\int_{B_v} \mathrm{Tr}\left(\delta_1 A^{(R)} \wedge \delta_2 A^{(R)} - \delta_2 A^{(R)} \wedge \delta_1 A^{(R)}\right) \tag{47}$$

Over a finite horizon slab $\Delta\mathcal{H} = [v_1, v_2]\times B_v$, the gauge-fixed matching functional is:

$$\gamma_H[P_{\mathrm{comp}}, e, \omega] = \frac{Mr_+}{4J}\frac{\int_{\Delta\mathcal{H}} P_{\mathrm{comp}}[\mathcal{Q}_3(\omega)]}{\int_{\Delta\mathcal{H}} \mathrm{CS}_3[A^{(R)}]} + \mathcal{O}\left(\frac{a^2}{M^2}\right) \tag{48}$$

Large gauge transformations $g : \mathcal{H} \to SU(2)$ shift the action by $8\pi^2 n$, quantizing $k \in \mathbb{Z}_{\geq 1}$ in the coherent state $Z^{\mathrm{comp}}_{\mathcal{H}} = \sum_{k\geq 1} e^{-(k-k^{\mathrm{cl}}_{\mathrm{eff}})^2/(2\sigma^2_H)} Z_{SU(2)_k}[\mathcal{H}]$.

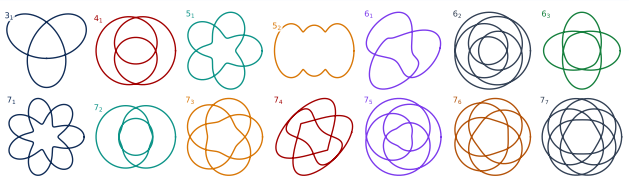


Figure 5: Complete low-complexity prime-knot basis $\mathcal{K}_{\leq 7} = \{3_1, 4_1, 5_1, 5_2, 6_1, 6_2, 6_3, 7_1, \ldots, 7_7\}$ with crossing numbers $c \leq 7$ (Fig. 1 of paper).

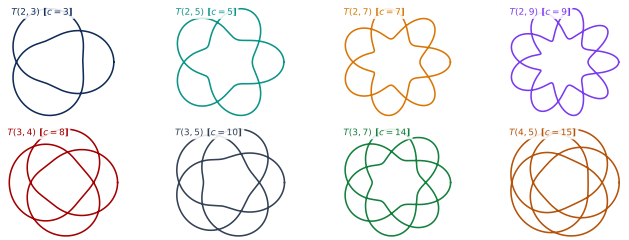


Figure 6: 3D projected embeddings of the structured torus-knot hierarchy $\mathcal{T}$ ($c[T(p,q)] \in \{3, 5, 7, 8, 9, 10, 14, 15\}$).

12. Wilson Loops & Torus-Knot Hierarchy

▸ Witten-Jones Knot Correspondence

A captured defect curve $\gamma \subset \mathcal{H}$ in representation $R = \text{fund}$ inserts a Wilson loop whose normalized amplitude equals the **Jones polynomial** $V_K(q)$ at root of unity $q_k = e^{2\pi i/(k+2)}$:

$$\mathcal{W}^{(\mathrm{fund})}_K(q_k) = \frac{Z_{\mathcal{H}}[K]}{Z_{\mathcal{H}}[\bigcirc]} = V_K(q_k), \quad \mathcal{I}_K(k) \equiv \ln|V_K(q_k)| \tag{49}$$

For the torus subfamily $T(2, 2n+1)$, $V_{T(2,2n+1)}(q) = q^n + \sum_{j=0}^{2n-1}(-1)^j q^{n+2+j}$, satisfying exact benchmarks $|V_{3_1}(q_1)| = |V_{3_1}(q_2)| = \lim_{k\to\infty}|V_{3_1}(q_k)| = 1$. For general torus knots $T(p,q)$ with $\gcd(p,q) = 1$, the minimal crossing number is $c[T(p,q)] = \min\{(p-1)q, (q-1)p\}$, giving $c = 3, 5, 7, 9$ for $T(2, 2n+1)$ and $c = 8, 10, 14, 15$ for $T(3,4), T(3,5), T(3,7), T(4,5)$.

Table 2: Exact Jones polynomials $V_K(q)$, log-amplitude diagnostics $\mathcal{I}_K(k)$ at $k = 5, 10$, and bounded comparison diagnostic $\ln\widehat{\Gamma}^{\mathrm{diag}}_K(k = 10)$ for $\mathcal{C}_{\mathrm{rep}}$.

K	Jones Polynomial $V_K(q)$	$\mathcal{I}_K(5)$	$\mathcal{I}_K(10)$	$\ln\widehat{\Gamma}^{\mathrm{diag}}_K$	Type
3_1	$q^{-1}+q^{-3}-q^{-4}$	+0.5673	+0.4094	−0.4695	Chiral
4_1	$q^{-2}-q^{-1}+1-q+q^2$	−0.3681	−1.3170	−3.9223	Amph.
5_1	$q^2+q^4-q^5+q^6-q^7$	+0.3876	+0.6315	−0.0254	Chiral
5_2	$q-q^2+2q^3-q^4+q^5-q^6$	+0.2503	+0.4792	−0.3299	Chiral
6_1	$q^{-2}-q^{-1}+2-2q+q^2-q^3+q^4$	+0.5185	−0.4439	−2.1762	Chiral
7_4	$q-2q^2+3q^3-2q^4+3q^5-2q^6+q^7-q^8$	+0.5787	+0.6442	0.0000	Chiral

▸ Torus-Knot Scaling & Topological Hierarchy

As the winding index n increases in $T(2, 2n+1)$, the Jones degree grows linearly ($d_{\max} = 3n+1$), shifting the first root-of-unity interference minimum toward higher Chern-Simons levels $k_{\mathrm{eff}} \sim 2(2n+1)$ and producing the diagonal resonance ridges in Fig. 7(b).

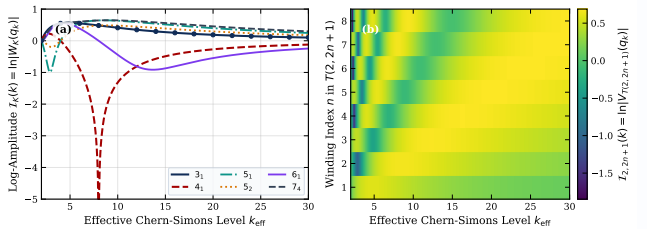


Figure 7: (a) Continuous k_{eff} envelopes of $\mathcal{I}_K(k) = \ln|W_K(q_k)|$ for $\mathcal{C}_{\mathrm{rep}}$, with integer $SU(2)_k$ sectors marked on 3_1. (b) Heatmap of $\mathcal{I}_{2,2n+1}(k)$ across k_{eff} and winding index $n \in [1, 8]$ for torus knots $T(2, 2n+1)$.

13. Conformal-Block Projector vs. Wilson Diagnostic

▸ Separating Quantum Amplitudes from Degeneracy

A central methodological advance of this work is separating **Wilson expectation amplitudes** from **microcanonical state counting**:

- **Why $|\mathcal{W}_K|$ is Not an Entropy Count:** $\mathcal{W}_K(q_k)$ is a path-integral amplitude. Deep negative valleys in $\mathcal{I}_K(k)$ occur when $V_K(q_k)$ passes near a root at $e^{2\pi i/(k+2)}$, not from state explosion.
- **Verlinde Conformal-Block Hilbert Space:** For a punctured S^2 horizon with spins $\{j_p\}$, the unconstrained dimension is governed by the modular S-matrix:

$$\dim \mathcal{H}_{k,\{j_p\}}(S^2) = \sum_{s=0}^{k/2} \frac{\prod_p S_{j_p s}}{(S_{0s})^{N-2}} \tag{50}$$

$$S_{js} = \sqrt{\frac{2}{k+2}} \sin\left[\frac{(2j+1)(2s+1)\pi}{k+2}\right] \tag{51}$$

- **Positive Conformal-Block Projector Π_K:** Given unconstrained density matrix $\rho_0 = e^{-\beta H_{\mathcal{H}}}$ and $Z_0 = \mathrm{Tr}\rho_0$, a knot constraint acts as a Hermitian projector $\Pi_K = \sum_{a\in\mathcal{A}_K} |a\rangle\langle a|$ ($0 \le \Pi_K \le \mathbf{1}$) onto admissible fusion channels $\mathcal{A}_K$:

$$Z_K^{\rm phys} = \mathrm{Tr}(\Pi_K \rho_0), \quad \Gamma_K^{\rm phys} = \frac{Z_K^{\rm phys}}{Z_0} = \frac{\mathrm{Tr}(\Pi_K\rho_0)}{\mathrm{Tr}\rho_0} \in [0,1] \tag{52}$$

$$\Delta S_K^{\rm phys} = \ln \Gamma_K^{\rm phys} \le 0, \quad \widehat{\Gamma}_K^{\rm diag} = \frac{|\mathcal{W}_K(q_k)|^2}{\max_{K'\in\mathcal{C}} |\mathcal{W}_{K'}(q_k)|^2} \le 1 \tag{53}$$

▸ Admissible Fusion Channels & State Truncation

At level k, primary fields carry integrable spins $j \in \{0, \frac{1}{2}, 1, \ldots, \frac{k}{2}\}$ obeying $SU(2)_k$ fusion rules $j_1 \otimes j_2 = \bigoplus_{j=|j_1-j_2|}^{\min(j_1+j_2, k-j_1-j_2)} j$. The projector Π_K restricts the trace to fusion paths $\mathcal{A}_K$ compatible with the knot framing and braiding, ensuring $0 \le \Gamma_K^{\rm phys} \le 1$ and strictly positive entropy loss $\Delta S_K^{\rm loss} = -\ln \Gamma_K^{\rm phys} \ge 0$.

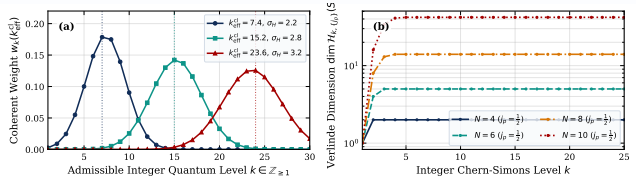


Figure 8: (a) Coherent-state Gaussian weights $w_k(k_{\rm eff}^{\rm cl})$ over integer levels $k \in \mathbb{Z}_{\ge 1}$. (b) Unconstrained Verlinde dimension $\dim \mathcal{H}_{k,\{1/2\}^N}(S^2)$ vs. k for $N = 4, 6, 8, 10$ punctures.

14. Primordial Defect Capture Prior for PBHs

▸ Two-Channel Cosmic-String Capture Model

For a PBH formed at radiation-era time t_f with horizon mass $M_H(t_f) = (2GH_f)^{-1} \simeq t_f/G$, collapse efficiency $\gamma_{\rm col} \in (0,1)$, mass $M_{\rm PBH} = \gamma_{\rm col} M_H(t_f)$, spin $\chi = J/M_{\rm PBH}^2$, and outer horizon radius $r_+ = M(1+\sqrt{1-\chi^2})$, the spin selector and area factor are:

$$\frac{J}{Mr_+} = \frac{\chi}{1+\sqrt{1-\chi^2}}, \quad r_+^2 H_f^2 = \frac{\gamma_{\rm col}^2}{4}\left(1+\sqrt{1-\chi^2}\right)^2 \tag{54}$$

During the capture window $\Delta t_f = \eta_t H_f^{-1}$, cosmic-string capture separates into:

1. **Closed String Loops** ($n_{\rm loop} = \nu_{\rm loop}/\ell_{\rm loop}^3$, $\ell_{\rm loop} = \zeta_\ell H_f^{-1}$, $\sigma_{\rm cap} = \zeta_{\rm cap}\pi r_+^2$):

$$\mu_{\rm loop}(M,\chi;t_f) = \frac{\nu_{\rm loop}\eta_t\zeta_{\rm cap}v_{\rm rel}}{\zeta_\ell^3}\pi r_+^2 H_f^2 \tag{55}$$

2. **Long Cosmic Strings** ($\ell_{\rm str} = \nu_{\rm str}/L_c^2$, $L_c = \zeta_c H_f^{-1}$, $A_{\rm sweep} = 4\pi\zeta_{\rm sweep} r_+^2 v_{\rm rel}\Delta t_f H_f$):

$$\mu_{\rm long}(M,\chi;t_f) \simeq \ell_{\rm str} A_{\rm sweep} = \frac{4\pi\nu_{\rm str}\eta_t\zeta_{\rm sweep}v_{\rm rel}}{\zeta_c^2} r_+^2 H_f^2 \tag{56}$$

With total mean $\mu_{\rm cap} = \mu_{\rm loop} + \mu_{\rm long}$, dilute Poisson distribution $P_N = e^{-\mu_{\rm cap}}\mu_{\rm cap}^N/N!$, and branching $P(K|N) = p_K(N)$, the ensemble partition function, thermodynamic entropy, and end-to-end map are:

$$Z_{\rm hor}^{\rm PBH} = \sum_K P(K|M,\chi,t_f) Z_K(k_{\rm eff}^{\rm cl}), \; S_{\rm hor}^{\rm PBH} = (1-\beta\partial_\beta)\ln Z \tag{57}$$

$$(t_f,\chi) \to \mu_{\rm loop}+\mu_{\rm long} \to P(K|M,\chi,t_f) \to Z_{\rm hor}^{\rm PBH} \tag{58}$$

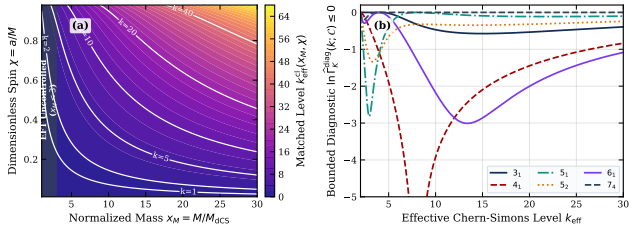


Figure 9: (a) Mass-spin-level map $k_{\rm eff}^{\rm cl}(x_M,\chi)$ for $\Lambda_H = 0.22 x_M$, showing integer $SU(2)_k$ contours and EFT cutoff $x_M < 3$. (b) Bounded diagnostic $\ln \widehat{\Gamma}_K^{\rm diag}(k;\mathcal{C}_{\rm rep}) \le 0$ vs. $k_{\rm eff}$.

15. EFT-Limited Evaporation-Envelope Sensitivity

▸ Competing Spin Dependencies & Hawking Envelope

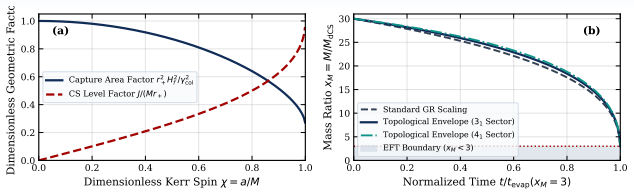


Figure 10: (a) Opposite spin dependence of the capture area factor $r_+^2 H_f^2/\gamma_{\rm col}^2$ (decreasing with χ) vs. CS level selector $J/(Mr_+)$ (increasing with χ). (b) EFT-limited Hawking evaporation trajectories $x_M(t)$ integrated down to $x_M = 3$.

▸ Thermodynamic Envelope & Remnant Conditions

In a fixed topological sector K, the conditional thermodynamic envelope entropy, envelope temperature $T_{\rm env}$, and heat capacity $C_{\rm env}$ are:

$$S_{\rm env}(M,J;K) = \frac{A_H(M,J)}{4G_{\rm eff}(\phi_H)} + S_{\rm topo}(M,J) + \ln\Gamma_K^{\rm phys}(k_{\rm eff}) \tag{59}$$

$$\frac{1}{T_{\rm env}} = \left(\frac{\partial S_{\rm env}}{\partial M}\right)_{J,K}, \quad C_{\rm env} = -\frac{(\partial_M S_{\rm env})^2}{\partial_M^2 S_{\rm env}} \tag{60}$$

The modified Stefan-Boltzmann evaporation ODE integrated down to $x_M = 3$ is:

$$\frac{dM}{dt} = -\frac{\epsilon_0}{M^2}\left(\frac{A_H}{A_H^{\rm Schw}}\right)\left(\frac{T_{\rm env}}{T_{\rm GR}}\right)^4 \tag{61}$$

A cold endpoint requires $T_{\rm env}(M_\star) \to 0$ and local stability requires $C_{\rm env}(M_\star) > 0$; neither follows universally from semiclassical dCS without UV input beyond $x_M < 3$.

▸ Evaporation Regimes & Endpoint Classification

Mass Window	Scaling	Thermodynamic Behavior
$x_M \gg 10$	$\zeta_{\rm CS} \ll 10^{-4}$	Standard Hawking $M(t) \propto (t_{\rm ev}-t)^{1/3}$
$3 \le x_M \le 10$	$\Delta S_K^{\rm phys} = \ln\Gamma_K^{\rm phys}$	Defect-projected $T_{\rm env}$ shift (controlled)
$x_M < 3$	$\zeta_{\rm CS} > 0.012$	EFT breakdown; UV completion required

Statistical Theorem: Topological State-Space Truncation
Captured topological defects act as quantum constraints that project the $SU(2)_k$ Verlinde Hilbert space onto admissible fusion channels ($\Delta S_K^{\rm phys} = \ln\Gamma_K^{\rm phys} \le 0$). Competing spin dependencies in $r_+^2(\chi)$ and $J/(Mr_+)$ create a peaked rotational window for defect-modified PBH evaporation.

16. Phenomenological Chiral EMRI Response Ansatz

▸ Polarized Horizon Flux Ansatz

To quantify how horizon topological sectors imprint onto gravitational waves from circular Extreme-Mass-Ratio Inspirals (EMRIs, mass ratio $\eta = \mu/M \ll 1$, frequency variable $x \equiv (M\Omega_{\rm orb})^{2/3}$), we parameterize the leading absorbed horizon energy flux for right- and left-handed orbital orientations ($\rho_R = +1, \rho_L = -1$):

$$\dot{E}_H^A = \dot{E}_H^{\rm Kerr}\left[1 + (\beta_{\rm even} + \rho_A \beta_{\rm odd})\, x^{5/2}\right], \quad A \in \{R, L\} \tag{62}$$

- **Parity-Even Channel** $\beta_{\rm even}$**:** $\beta_{\rm even}(k, K) = b_\Omega \frac{\delta\Omega_H}{\Omega_H^{\rm GR}} + b_\Gamma\left[1 - \Gamma_K^{\rm phys}(k)\right] + \cdots$
- **Parity-Odd Chiral Channel** $\beta_{\rm odd}$**:** Controlled by the complex Wilson phase $\Theta_K(k) \equiv \arg \mathcal{W}_K(e^{2\pi i/(k+2)})$:

$$\beta_{\rm odd}(k, K) = \beta_0 \sin\Theta_K(k) \tag{63}$$

▸ Stationary-Phase Inspiral Dephasing

Over the fiducial LISA inspiral window $x \in [x_i, x_f] = [0.08, 1/6]$ (below $x_{\rm ISCO} = 1/6$), the horizon-flux perturbation shifts the gravitational-wave phase by:

$$\Delta\Psi^H_{R/L} = -\frac{5}{32\eta}\,(\beta_{\rm even} \pm \beta_{\rm odd}) \ln\left(\frac{x_f}{x_i}\right) \tag{64}$$

$$\Delta\Psi_R - \Delta\Psi_L = -\frac{5}{16\eta}\beta_0 \sin\Theta_K(k) \ln\left(\frac{x_f}{x_i}\right) \tag{65}$$

For the right-handed trefoil 3_1 ($V_{3_1} = q^{-1} + q^{-3} - q^{-4}$), $\beta_0 = 5 \times 10^{-6}$, $\eta = 10^{-5}$, and $\ln((1/6)/0.08) \approx 0.73397$, the exact polarized phase shifts are $\Delta\Psi_R = -0.28671$ rad, $\Delta\Psi_L = -0.17202$ rad, and $\mathbf{\Delta\Psi_R - \Delta\Psi_L = -0.11468\ rad}$, well within LISA matched-filtering phase sensitivity ($\delta\Psi_{\rm LISA} \sim 0.1$ rad at SNR ~ 30).

▸ Benchmark EMRI Dephasing Across Knot Topologies ($\eta = 10^{-5}$)

Sector K	$\Delta\Psi_R$ [rad]	$\Delta\Psi_L$ [rad]	$\Delta\Psi_R - \Delta\Psi_L$	Signature
3_1 $(k=5)$	-0.2867	-0.1720	-0.1147 rad	Chiral split
$\overline{3}_1$ $(k=5)$	-0.1720	-0.2867	$+0.1147$ rad	Mirror flip
4_1 $(\forall k)$	-0.2294	-0.2294	0.0000 rad	Amphichiral

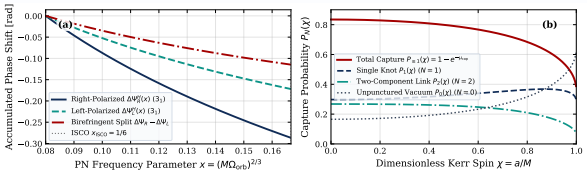


Figure 11: (a) Cumulative phase shifts $\Delta\Psi^H_{R/L}(x)$ and split $\Delta\Psi_R - \Delta\Psi_L$ across $x \in [0.08, 1/6]$. (b) Poisson capture probabilities $P_N(\chi)$ vs. spin χ.

17. Chiral Splitting Map & Parameter Disentanglement

▸ Chirality Selection & Mirror Inversion

Reversing spacetime orientation or replacing a knot K with its mirror image $\overline{K}$ ($q \to q^{-1}$) flips $\Theta_K \to -\Theta_K$ and reverses the sign of $\Delta\Psi_R - \Delta\Psi_L$. By contrast, amphichiral knots such as the figure-eight knot 4_1 satisfy $V_{4_1}(q) = V_{4_1}(q^{-1}) \in \mathbb{R}$, yielding $\sin\Theta_{4_1} \equiv 0$ and **identically zero chiral phase splitting!**

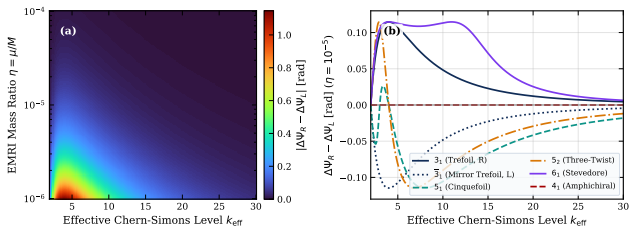


Figure 12: (a) Birefringent EMRI phase split $|\Delta\Psi_R - \Delta\Psi_L|$ [rad] across $(k_{\rm eff}, \eta)$ for 3_1 ($\beta_0 = 5 \times 10^{-6}$). (b) Chiral phase splitting $\Delta\Psi_R - \Delta\Psi_L$ at $\eta = 10^{-5}$ comparing chiral knots $(3_1, 5_1, 5_2, 6_1)$, mirror trefoil $\overline{3}_1$ (sign inversion), and amphichiral 4_1 (identically zero).

▸ Breaking Parameter Degeneracies in LISA Waveforms

Environmental accretion, modified Kerr quadrupole moments, and horizon absorption are often degenerate in single-polarization EMRI templates [58, 59]. Comparing prograde/retrograde or right/left-handed polarizations isolates $\Delta\Psi_R - \Delta\Psi_L \propto \eta^{-1}\sin\Theta_K(k)$, which depends solely on the chiral Wilson phase and vanishes identically for parity-even environments.

Table 3: Orthogonal scaling laws and physical roles of the four horizon response observables.

Horizon Observable	Scaling Law	Physical & Observational Role
Compact Level $k_{\rm eff}^{\rm cl}$	$4\pi\Lambda_H \frac{\chi}{1+\sqrt{1-\chi^2}}$	Selects integer $SU(2)_k$ quantum sector via spin χ
Frame-Dragging Shift	$\frac{\delta\Omega_H}{\Omega_H^{\rm GR}} = \frac{709}{7168} x_M^{-4}$	Parity-even shift of superradiant threshold $\omega = m\Omega_H$
Projector Entropy $\Delta S_K^{\rm phys}$	$\ln\Gamma_K^{\rm phys}(k_\star) \le 0$	Modifies Hawking temperature $T_{\rm env}$ & heat capacity
Chiral EMRI Split	$-\frac{5\beta_0}{16\eta}\sin\Theta_K \ln\frac{x_f}{x_i}$	Parity-odd birefringent phase shift ($=0$ for amphichiral 4_1)

18. Summary of Core Contributions & References

▸ Five Pillars of This Work

1. **Self-Consistent Slow-Rotation Hierarchy:** Derived the dipolar scalar $\Phi_{\rm phys}(r)$ and frame-dragging shift $\omega_{\rm CS}(r)$ in a single Planck-normalized action, proving exact equivalence with standard dCS conventions and establishing the EFT bound $x_M = M/M_{\rm dCS} \gtrsim 3$.
2. **Wald-Noether Normal-Bundle Charge:** Proved that the scalar-Pontryagin interaction induces a boost-invariant horizon normal-bundle curvature charge $S_{\rm topo} = \frac{\alpha}{4G}\oint\sqrt{q}\xi F_N$. Evaluated $F_N^{(0)} = 2\,\mathrm{Im}\,\Psi_2^{\rm Kerr}|_{r_+}$ on Kerr and derived the 2nd-order Raychaudhuri topological flux $\langle\mathcal{F}^{(2)}_{\rm topo}\rangle$.
3. **Conditional Compact $SU(2)_k$ Boundary Model:** Formulated the gauge-fixed compact projection $\mathcal{P}_{\mathcal{H}}$, presymplectic matching functional γ_H, large-gauge level quantization $k \in \mathbb{Z}_{\ge 1}$, and coherent-state superposition $Z_{\mathcal{H}}^{\rm comp}$.
4. **Projector Truncation vs. Wilson Diagnostics:** Separated conformal-block projectors $\Gamma_K^{\rm phys} = \mathrm{Tr}(\Pi_K\rho_0)/\mathrm{Tr}\rho_0 \le 1$ from bounded Jones diagnostics $\widehat{\Gamma}_K^{\rm diag}$, connecting primordial string capture ($\mu_{\rm loop} + \mu_{\rm long}$) to EFT-limited evaporation sensitivity and chiral EMRI phase splitting.
5. **Next Frontier:** Solving the fully coupled dynamical Kerr-dCS Teukolsky-like perturbation equations to calibrate the noncompact dissipative flux and determine β_0 from first principles.

▸ Methodological Scope & Open Frontiers

Domain / Assumption	Current Status & Next Step
Perturbative Control	Controlled for $\chi \ll 1, \zeta_{\rm CS} \ll 1$ ($x_M \gtrsim 3$)
Boundary Gauge $\mathcal{P}_{\mathcal{H}}$	Adiabatic slab; extend to dynamical shear
EMRI Coupling β_0	Calibrate via coupled Kerr-dCS Teukolsky solver
Prior $p_K(N)$	Extract from cosmological string-network sims

▸ Selected References

- **dCS Gravity & Rotating Black Holes:** R. Jackiw & S.-Y. Pi, *PRD* **68**, 104012 (2003); S. Alexander & N. Yunes, *Phys. Rep.* **480**, 1 (2009); N. Yunes & F. Pretorius, *PRD* **79**, 084043 (2009); K. Yagi, N. Yunes & T. Tanaka, *PRL* **109**, 251105 (2012); L. C. Stein, *PRD* **90**, 044061 (2014).
- **Wald Charge & Horizon TQFT:** R. M. Wald, *PRD* **48**, R3427 (1993); V. Iyer & R. M. Wald, *PRD* **50**, 846 (1994); Y. Tachikawa, *CQG* **24**, 737 (2007); E. Witten, *CMP* **121**, 351 (1989); A. Ashtekar, J. C. Baez & K. Krasnov, *ATMP* **4**, 1 (2000); J. Engle, K. Noui, A. Perez & D. Pranzetti, *PRD* **82**, 044050 (2010).
- **PBH Defects & LISA EMRIs:** B. Carr *et al.*, *Phys. Rep.* **1054**, 1 (2024); S. Babak *et al.*, *PRD* **95**, 103012 (2017); L. Barack *et al.*, *CQG* **36**, 143001 (2019).

Author Contact & Affiliation
Xiatong Li and **Jingxu Wu** (wuxj@my.msu.ru)
Faculty of Physics, Lomonosov Moscow State University, Moscow 119991, Russia